ARTICLES
https://doi.org/10.1038/s41563-019-0495-0
nature materials

Reversible coordinative binding and separation of sulfur dioxide in a robust metal–organic framework with open copper sites

Gemma L. Smith[1,8], Jennifer E. Eyley[1,8], Xue Han[1], Xinran Zhang[1], Jiangnan Li[1], Nicholas M. Jacques[1], Harry G. W. Godfrey[1], Stephen P. Argent[2], Laura J. McCormick McPherson[3], Simon J. Teat[3], Yongqiang Cheng[4], Mark D. Frogley[5], Gianfelice Cinque[5], Sarah J. Day[5], Chiu C. Tang[5], Timothy L. Easun[6], Svemir Rudić[7], Anibal J. Ramirez-Cuesta[4], Sihai Yang[1*] and Martin Schröder[1*]

Emissions of SO_2 from flue gas and marine transport have detrimental impacts on the environment and human health, but SO_2 is also an important industrial feedstock if it can be recovered, stored and transported efficiently. Here we report the exceptional adsorption and separation of SO_2 in a porous material, [Cu_2(L)] (H_4L = 4′,4‴-(pyridine-3,5-diyl)bis([1,1′-biphenyl]-3,5-dicarboxylic acid)), MFM-170. MFM-170 exhibits fully reversible SO_2 uptake of 17.5 mmol g^{-1} at 298 K and 1.0 bar, and the SO_2 binding domains for trapped molecules within MFM-170 have been determined. We report the reversible coordination of SO_2 to open Cu(II) sites, which contributes to excellent adsorption thermodynamics and selectivities for SO_2 binding and facile regeneration of MFM-170 after desorption. MFM-170 is stable to water, acid and base and shows great promise for the dynamic separation of SO_2 from simulated flue gas mixtures, as confirmed by breakthrough experiments.

The use of fossil fuels represents a major contribution to many serious environmental issues, but the transition to clean energy sources remains challenging as new technologies mature. The release of SO_2, for which anthropogenic sources account for >87% of global emissions[1], has detrimental effects on the environment and human health, but SO_2 is also an important feedstock for sulfuric acid production. Furthermore, trace SO_2 can greatly reduce the activity of amine-based CO_2 scrubbers[2] and can irreversibly poison catalysts for selective NO_x reduction[3] and CH_4 combustion[4].

In recent years, there has been growing interest in the development of dry regenerable sorbents of SO_2 operating under ambient conditions[5–7]. These materials offer advantages over existing wet flue gas desulfurization (FGD) technologies by reducing energy and water requirements and minimizing waste. The regeneration of sorbents allows the recovery of saleable SO_2, which can be further used via conversion to elemental sulfur or sulfuric acid[8]. High-capacity sorbents for SO_2 can also be used for the safe transportation of recovered gaseous SO_2 under ambient conditions without the large energy demands required for pressurization.

Porous metal–organic framework (MOF) materials have been studied extensively for uptake and separation of a wide variety of gases, notably CO_2, H_2 and hydrocarbons[9–14], but their application to SO_2 capture has been hindered by the toxic and corrosive nature of this substrate. To date, several MOFs have been tested as SO_2 adsorbents (Supplementary Table 1)[15–25], but many exhibit limited stability and/or reversibility under near-ambient conditions. Current top-performing MOFs for SO_2 adsorption at 298 K and 1.0 bar include MFM-202a (10.2 mmol g^{-1}; ref. [18]) and SIFSIX-1-Cu (11.0 mmol g^{-1}; ref. [16]). The former is subject to an irreversible phase change in framework structure on SO_2 uptake, while the steep uptake of the latter may render it unfeasible for practical pressure-swing adsorption applications[26,27]. Ideal sorbents for use in FGD processes should have low energy penalties for regeneration and high SO_2/CO_2 selectivity at low concentrations of SO_2 (~2,000 ppm). Open metal sites (OMSs) can improve gas binding selectivity, but the resultant MOFs are often subject to framework degradation on contact with water, precluding their practical application[28–31].

Here, we report the reversible coordinative binding of SO_2 to open Cu(II) sites in a remarkably robust material, MFM-170, leading to optimal adsorption and selectivity for SO_2. Coordination of the pyridyl N donor to one axial site of the $Cu_2(O_2CR)_4$ paddle-wheel unit leads to an unusual (3,36)-connected *txt* framework that, on removal of axial water, affords one open Cu(II) site per $Cu_2(O_2CR)_4$ unit. At 298 K and 1.0 bar, MFM-170 exhibits an unprecedented uptake of SO_2 of 17.5 mmol g^{-1}, fully reversible at ambient temperature. The high selectivity of MFM-170 for SO_2 has been probed by in situ single-crystal X-ray diffraction, Fourier transform infrared (FTIR) microspectroscopy and inelastic neutron scattering (INS). Breakthrough experiments with simulated flue gas mixtures demonstrate that MFM-170 has excellent separation properties, even in the presence of water and at elevated temperatures. The stability of MFM-170 to wet SO_2 has been confirmed by long-duration synchrotron X-ray powder diffraction experiments.

Synthesis and structural analysis of MFM-170•solv

Solvothermal reaction of the pyridine-containing tetracarboxylate linker 4′,4‴-(pyridine-3,5-diyl)bis([1,1′-biphenyl]-3,5-dicarboxylic

[1]School of Chemistry, University of Manchester, Manchester, UK. [2]School of Chemistry, University of Nottingham, Nottingham, UK. [3]Advanced Light Source, Lawrence Berkeley National Laboratory, Berkeley, CA, USA. [4]Oak Ridge National Laboratory, Oak Ridge, TN, USA. [5]Diamond Light Source, Harwell Science Campus, Didcot, UK. [6]School of Chemistry, Cardiff University, Cardiff, UK. [7]ISIS, STFC Rutherford Appleton Laboratory, Chilton, UK. [8]These authors contributed equally: Gemma L. Smith, Jennifer E. Eyley. *e-mail: sihai.yang@manchester.ac.uk; m.schroder@manchester.ac.uk

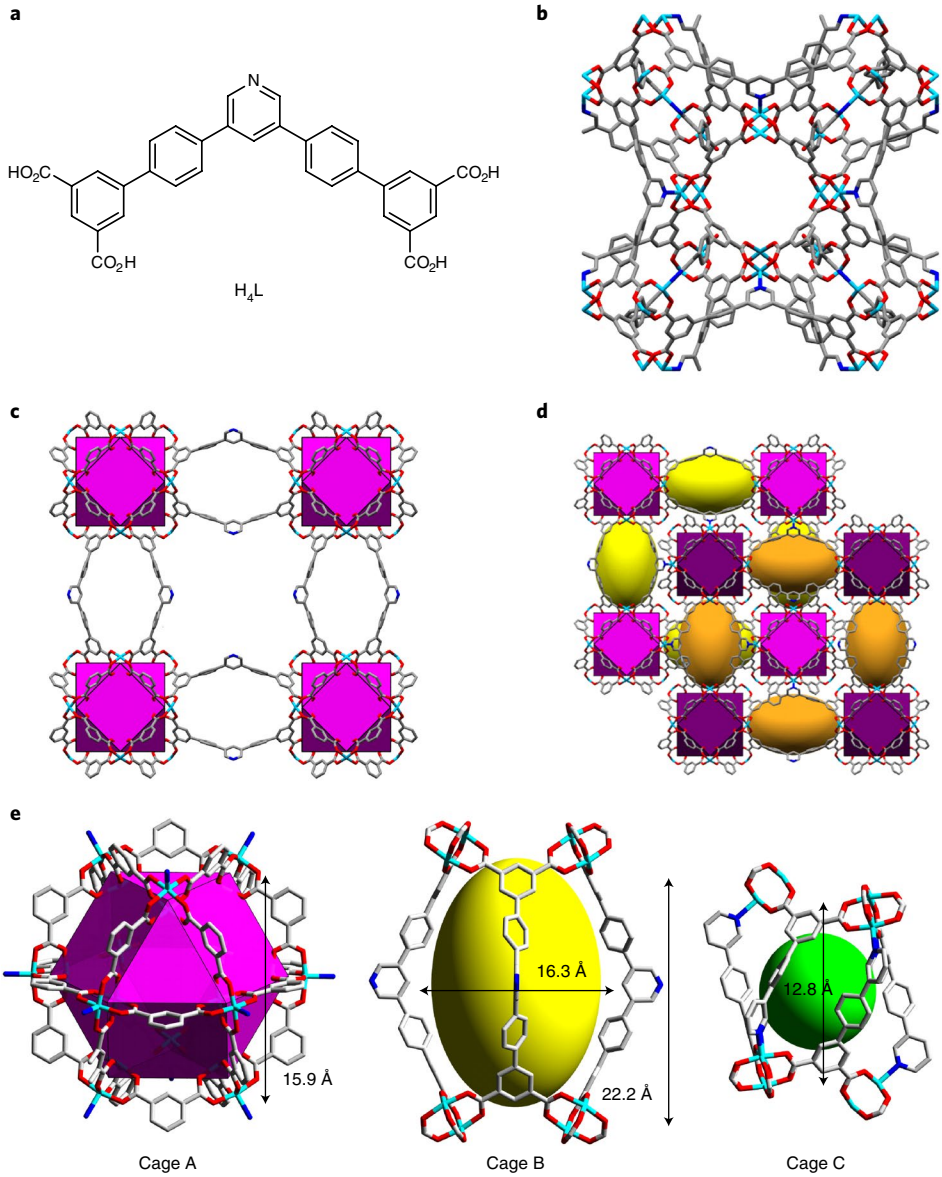

Fig. 1 | Structure of MFM-170 from single-crystal X-ray diffraction data. a, The structure of H_4L. **b**, The unit cell of MFM-170. **c**, The simplified structure showing the smaller net of MFM-170. **d**, The full structure of MFM-170 resulting from the connection of the two smaller nets. **e**, Metal-ligand cages A, B and C observed in MFM-170. The metal cluster of MFM-170 consists of a $[Cu_2(O_2CR)_4]$ paddle wheel with four isophthalate units occupying the equatorial sites and one pyridyl N donor from the ligand coordinating to the axial site of one Cu(II) cation. The axial position of the other Cu(II) cation of the $Cu_2(O_2CR)_4$ unit is occupied by a water molecule. The framework is constructed from a $[Cu_{24}(RC_6H_3(CO_2)_2)_{24}]$ cuboctahedron, which acts as a 36-connected node, joined in a cubic array to six adjacent cuboctahedra by four ligands each. The overall framework can be visualized as this smaller cubic net, which is connected to a secondary identical net via the 12 corners of the cuboctahedra via Cu–N bonds. Thus, each ligand is a three-connected node, with two isophthalate moieties that each connect an edge of a cuboctahedron, and one pyridyl N atom that joins a corner of a cuboctahedron. Cu, cyan; C, grey; O, red; N, blue; void space is highlighted in pink, yellow, purple and orange.

acid) (H_4L; Fig. 1a, Supplementary Fig. 1) and $Cu(NO_3)_2{\bullet}2.5H_2O$ in a mixture of dimethylformamide (DMF) and H_2O (v/v = 5:1) under acidic conditions (HNO_3) yielded blue octahedral crystals of $[Cu_2(L)(H_2O)]{\bullet}6DMF$, denoted MFM-170•$H_2O$•solv. Single-crystal X-ray diffraction reveals that MFM-170•H_2O•solv crystallizes in the cubic space group *Im*-3*m* to form a rarely observed (3,36)-connected net with *txt* topology (Fig. 1b–d)[32–34]. The interconnected void spaces in MFM-170 can be considered as three distinct cages, denoted cages A, B and C in Fig. 1e. The metal–organic cuboctahedra (cage A) has a diameter of 15.9 Å, comprising alternating triangular and square faces. Each square face of cage A connects to a cage B, which is formed by four V-shaped linkers bowing outwards to create a prolate pore (width 16.3 Å and length 22.2 Å). Cage C is the smallest of the three, connects with the triangular faces of cage A, and measures 12.8 Å between opposite triangular faces and 14.2 Å between opposite C atoms.

Thermal and chemical stability of MFM-170

Thermogravimetric analysis of MFM-170•H_2O•solv shows thermal stability up to ~620 K, which is also confirmed by variable temperature powder X-ray diffraction (PXRD) analysis (Supplementary Figs. 4 and 8). The chemical robustness of MFM-170•H_2O•solv to a

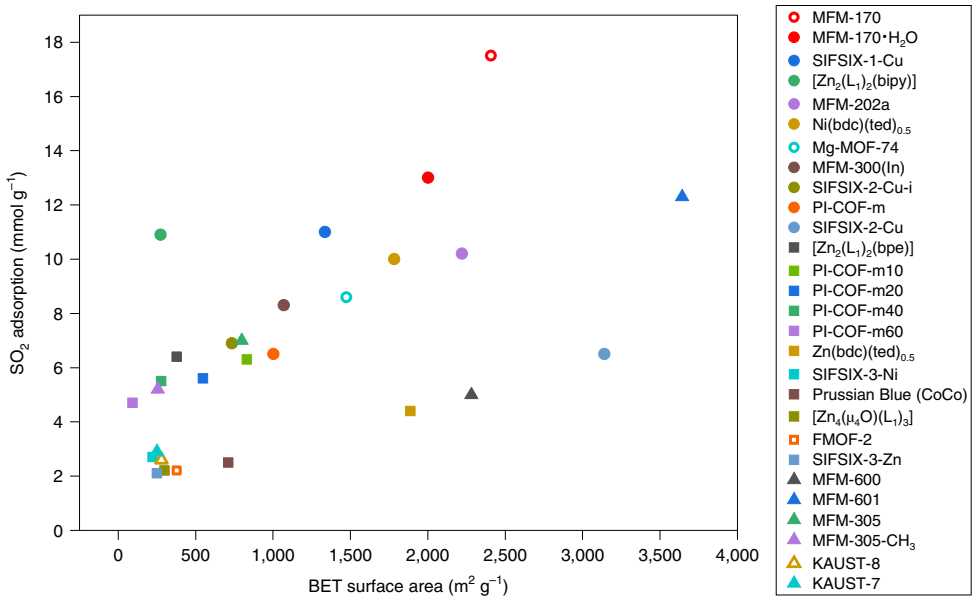

Fig. 2 | Comparison of SO_2 uptakes of reported MOFs and covalent-organic frameworks (COFs) at 1.0 bar and 298 K. Plot of SO_2 adsorption (at 1.0 bar and 298 K) against BET surface area. A general linear relationship between SO_2 uptake and BET surface area is observed. Open symbols denote the presence of OMSs in the MOF.

range of harsh environmental conditions was investigated, including suspending the sample in boiling water and aqueous solutions of pH between 2 and 12. No loss in crystallinity was observed by PXRD after exposure to these conditions (Supplementary Figs. 2, 3 and 6). Desolvated MFM-170 can be rehydrated to MFM-170•H_2O on contact with water without loss of crystallinity. Reversible water adsorption isotherms are shown in Supplementary Fig. 10. To assess the long-term stability of MFM-170 to humid SO_2 and water, synchrotron PXRD data were collected for wet SO_2-loaded MFM-170 samples every week for 10 weeks (Supplementary Fig. 7). Neither loss of crystallinity nor change in the structure of this material was observed (Supplementary Table 4), confirming the excellent chemical resilience of the framework. This is attributed to the unusual framework connectivity, whereby the axially coordinated pyridyl N donors interlock the two cubic nets and block one of the two axial Cu(II) sites.

Analysis of gas adsorption isotherms

Desolvated MFM-170 possesses a Brunauer–Emmett–Teller (BET) surface area of 2,408 $m^2 g^{-1}$, consistent with the calculated surface area of 2,456 $m^2 g^{-1}$ based on the single-crystal structure, and a pore volume of 0.88 $cm^3 g^{-1}$ (calculated from the N_2 isotherm at 77 K; Supplementary Fig. 9), consistent with a pore volume of 0.87 $cm^3 g^{-1}$ with solvent-accessible void space of 61%, derived from the single-crystal structure. MFM-170 shows an SO_2 uptake of 19.4 mmol g^{-1} (or 1.24 g g^{-1}) at 273 K and 1.0 bar. This represents a high SO_2 uptake capacity in porous materials, higher than MFM-601 (16.9 mmol g^{-1}; ref. [15]), MFM-202a (13.0 mmol g^{-1}; ref. [18]) and mesoporous silicate MCM-41 (11.6 mmol g^{-1}; ref. [35]) under the same conditions. The performance of state-of-the-art porous materials under ambient conditions is summarized in Supplementary Table 1 and Fig. 2. MFM-170 exhibits an SO_2 adsorption capacity of 17.5 mmol g^{-1} at 298 K and 1.0 bar, which exceeds the current leading MOFs, such as MFM-601 (12.3 mmol g^{-1}; ref. [15]), SIFSIX-1-Cu (11.0 mmol g^{-1}; ref. [16]), $[Zn_2(L_1)_2(bipy)]$ (10.9 mmol g^{-1} at 293 K; ref. [17]) and Ni(bdc)$(ted)_{0.5}$ (10.0 mmol g^{-1}; ref. [19]). Furthermore, MFM-170 shows high SO_2 adsorption at elevated temperatures (11.6 mmol g^{-1} at 333 K and 1 bar; Fig. 3b). The uptake of SO_2 in MFM-170 shows a reversible type I isotherm with high uptakes at low pressure (Fig. 3): at 273 K the uptake at 0.03 bar is 6.5 mmol g^{-1}. Despite the high uptake at low pressure, the excellent reversibility of the SO_2 isotherms at 273–333 K indicates that MFM-170 can be fully regenerated under pressure-swing conditions. No loss of adsorption capacity of SO_2 was detected in MFM-170 after 50 adsorption–desorption cycles at 298 K (Fig. 4a), and PXRD analysis of MFM-170 after these cycles confirms the full retention of the crystal structure (Fig. 4b).

To probe the effect of the OMSs on SO_2 uptake, isotherms were measured for the coordinatively saturated parent material, MFM-170•H_2O, in which a water molecule is retained at the Cu(II) site. The SO_2 isotherm of MFM-170•H_2O at 273 K shows a reduced but still exceptionally high uptake of SO_2 (16.2 mmol g^{-1}; Supplementary Fig. 15). The difference in adsorption at 1.0 bar between MFM-170•H_2O and MFM-170 corresponds to approximately twice the density of open Cu(II) sites (1.46 mmol g^{-1}), suggesting that OMSs have a key role in promoting SO_2 uptake.

MFM-170 shows an uptake of only 3.04 mmol g^{-1} of CO_2, 1.33 mmol g^{-1} of CH_4, 0.38 mmol g^{-1} of CO and 0.28 mmol g^{-1} of N_2 at 1 bar and 298 K (Fig. 3a, Supplementary Figs. 11–14). The selectivities of MFM-170 for SO_2/CO_2, SO_2/N_2, SO_2/CO and SO_2/CH_4 were calculated from single-component isotherms at 298 K (Supplementary Figs. 19 and 20). Owing to the negligible interaction of N_2 with the framework, MFM-170 exhibits a high selectivity of 944 based on ideal adsorbed solution theory (IAST) for an equimolar mixture of SO_2/N_2 at 1.0 bar. MFM-170 also shows high selectivity values of 260, 203 and 35 for equimolar mixtures of SO_2/CH_4, SO_2/CO and SO_2/CO_2, respectively. Considering the relatively low concentrations of SO_2 present in flue gas, decreasing the SO_2/X ratio from 50:50 to 1:99 still affords high selectivity values for SO_2/N_2 (260) and SO_2/CO_2 (28). These values are lower than those reported for SIFSIX-2-Cu-i (ref. [16]), which possesses narrower pores than MFM-170.

Determination of the binding domains for adsorbed SO_2

The binding domains of SO_2 were studied using in situ synchrotron single-crystal X-ray diffraction. Structural analysis of desolvated MFM-170 confirms the complete removal of free solvents in the

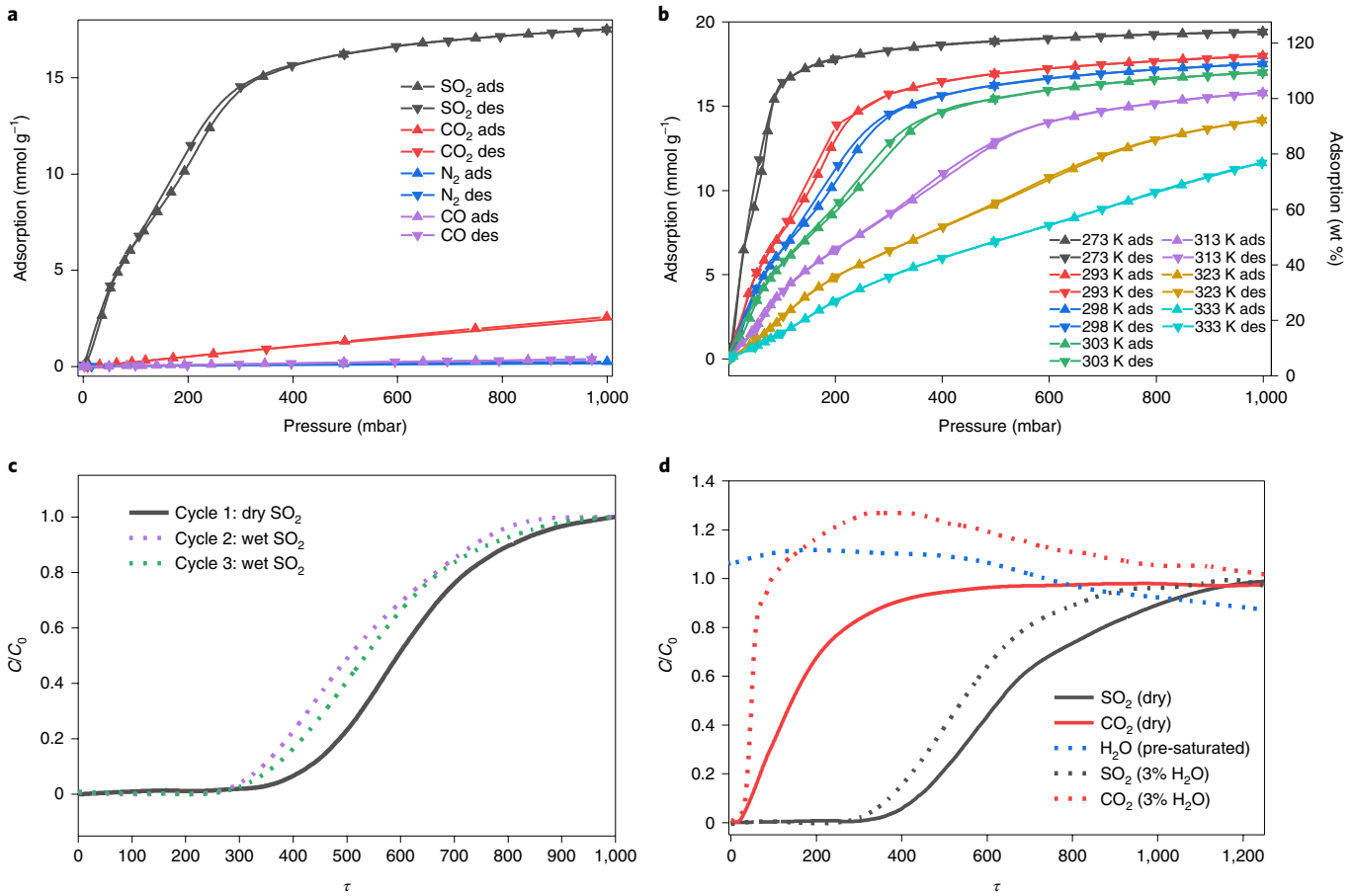

Fig. 3 | Gas sorption and separation properties of MFM-170. a, Adsorption (ads) and desorption (des) isotherms for MFM-170 at 298 K up to 1 bar for SO_2, CO_2, N_2 and CO. At 298 K and 1.0 bar, the volumetric storage density of SO_2 in MFM-170 is 307 times that of gaseous SO_2 under the same conditions, or 75 times of that of compressed SO_2 at a pressure of 3.9 bar in a pressure vessel (packing efficiency and system volume are not taken into consideration). **b**, SO_2 adsorption and desorption isotherms for MFM-170 at 273–333 K and up to 1 bar. The wt % is in terms of SO_2(g)/MOF(g). **c**, Breakthrough curves for SO_2 at 298 K under dry and wet conditions. *C* is the gas concentration of SO_2 and CO_2 at the outlet, and C_0 is the corresponding inlet concentration. $C/C_0 = 1$ indicates complete breakthrough. The consistency in the retention time for SO_2 under wet conditions confirms the high stability of MFM-170. The dry conditions were 99.75% He and 2,500 ppm SO_2. The wet conditions were 98.25% He, 1.5% H_2O and 2,500 ppm SO_2. The flow rate was 26 ml min^{-1}. **d**, A comparison of the binary SO_2/CO_2 dynamic separations at 298 K under dry and wet conditions. The dry sample was first activated under a flow of He at 423 K, and the subsequent gas mixture composition was 84.75% He, 15% CO_2 and 2,500 ppm SO_2 at a total flow rate of 26 ml min^{-1}. For experiments under wet conditions, the bed was first exposed to a flow of 3% H_2O in He until the breakthrough of water was achieved (not shown). The subsequent gas mixture composition was ~81.6% He, 18% CO_2 and 4,050 ppm SO_2 with a total flow rate of 16 ml min^{-1}. Owing to the experimental set-up, He was used instead of N_2 as a non-interacting component. τ is equal to $tu/\varepsilon L$, where *t* is the actual breakthrough time, *u* is the gas velocity, ε is the fractional porosity and *L* is the length of the fixed bed. See the Supplementary Information for details.

pore and the bound water molecule on the Cu(II) sites, generating 12 open Cu(II) sites on the internal surface of cage A. Refinement of the diffraction data for the SO_2-loaded sample at 298 K revealed significant residual electron densities, which were sequentially assigned to six distinct binding sites 1–6 in order of decreasing occupancy, giving a formula of $[Cu_2(L)(SO_2)_{0.67}](SO_2)_{4.79}$ (denoted MFM-170•5.46SO_2; Fig. 5).

The primary binding site, 1, is situated on a three-fold rotational axis in the triangular window of cage A and has full occupancy (Fig. 5b). The S_{SO_2} atom points towards the $[Cu_2(O_2CR)_4]$ paddle wheel, forming close contacts to two carboxylate O centres $[S_{SO_2}(\delta^+)\cdots(\delta^-)O = 3.16(3)$ Å]. Simultaneously, the O_{SO_2} atom located at the centre of the window forms a three-fold interaction to the isophthalate C–H groups lining the window $[O_{SO_2}\cdots C = 4.18(3)$ Å < O•••H–C = 140.5(6) Å]. SO_2(2) is coordinated to the open Cu(II) site in an end-on manner $[O_{SO_2}$–Cu = 2.28(10) Å] with an occupancy of 0.67. The O_{SO_2}–Cu bond distance is shorter than the sum of the van der Waals radius of Cu and O (2.92 Å). The two O_{SO_2} atoms are parallel to the Cu•••Cu axis, while the S_{SO_2} is disordered about a C_2 axis. This is the first crystallographic example of SO_2 coordination to OMSs within a MOF. The Cu(II) centre is not the most occupied site, which is at least in part due to steric hindrance created by site 1; the 12 Cu(II) sites line the internal surface of cage A and are therefore accessed through the square faces, as the triangular windows are fully occupied by SO_2 molecules.

SO_2(3) (occupancy = 0.47) is located in a crevice between cage B of one net and a perpendicular cage B of the second net (Fig. 5b). This small pocket accommodates interactions with the face of the pyridine ring $[S_{SO_2}\cdots N = 3.48(18)$ Å] and phenyl H atoms $[O_{SO_2}\cdots C^4 = 3.20(4)$ Å, $O_{SO_2}\cdots C^{11} = 4.80(4)$ Å], accounting for ~30% of all located SO_2 molecules. SO_2(4) (occupancy = 0.32) is in cage C and situated with the S atom facing the carboxylate oxygens of the paddle wheel $[S_{SO_2}(\delta^+)\cdots(\delta^-)O^1 = 3.67(3)$ Å] and interacts with neighbouring phenyl rings $[O_{SO_2}\cdots C^7 = 3.70(5)$ Å,

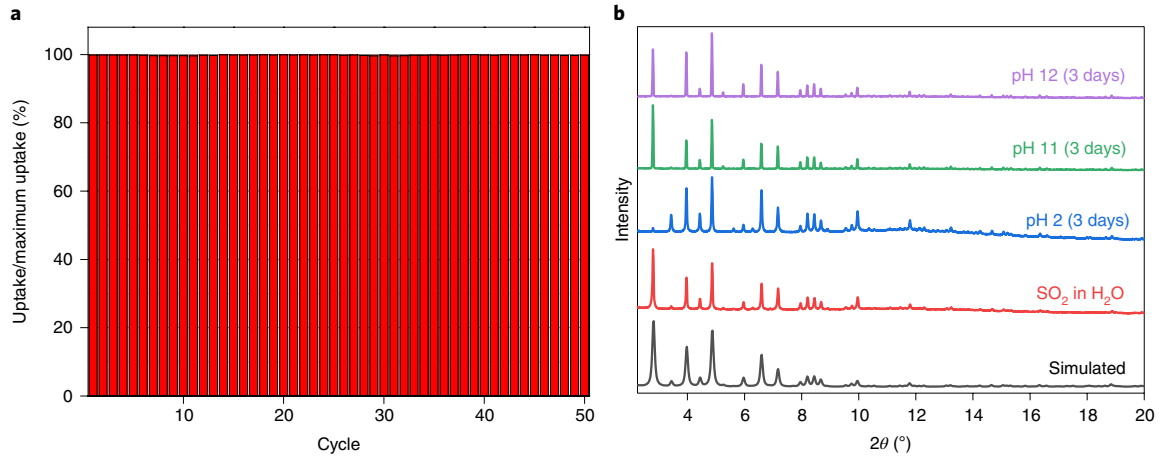

Fig. 4 | Chemical stability tests for MFM-170. a, Fifty adsorption–desorption cycles for SO_2 in MFM-170 at 298 K. All SO_2 was fully desorbed under dynamic vacuum at 298 K between cycles, and no loss of uptake capacity was observed. **b**, PXRD analysis of MFM-170 exposed to various external conditions. Changes in intensities of Bragg peaks correspond to the inclusion of guest species in the pores of MFM-170. Pawley refinements are shown in the Supplementary Information.

$O_{SO_2} \cdots$ ring centroid = 3.26(5) Å]. SO_2(5) is in the square face between cages A and B with an occupancy of 0.26 and dipole interactions between the adsorbed SO_2 molecules are also observed [$S_{SO_2(2)} \cdots O_{SO_2(5)}$ = 2.54(6) Å, $O_{SO_2(5)} \cdots S_{SO_2(6)}$ = 2.88(5) Å]. The least populated site, 6 (occupancy = 0.23), is sandwiched between two phenyl rings in cage C and forms interactions between the S(δ^+) and the phenyl π electrons at distances of 3.28(15) Å and 3.30(15) Å, measured between the ring centroids and S_{SO_2}.

We sought to examine the most thermodynamically favoured site via controlled desorption of MFM-170•5.46SO_2. Diffraction data collected for the sample under a dynamic vacuum at 298 K showed that almost all adsorbed SO_2 molecules were removed from the structure of MFM-170, leaving just the Cu(II)-bound SO_2(2) with an occupancy of 0.09. This confirms that the Cu(II) site is indeed the thermodynamically strongest binding site, but is sufficiently weak to be almost entirely desorbed on reduction of pressure. Density functional theory (DFT) calculations indicated that for MOF-74(*M*) (*M* = Mg, Ni, Co, Zn), the sites with highest binding energies for SO_2 were located at the OMSs[36]. For MFM-170, the multi-site cooperative binding between SO_2 molecules (Fig. 5c) results in an optimal balance of high selectivity and excellent reversibility for SO_2 adsorption. Subsequent brief heating to 400 K fully regenerated MFM-170 without any loss of crystallinity.

To investigate the nature of SO_2 binding in the absence of OMSs, a single crystal of MFM-170•H_2O•solv was activated under mild conditions to remove free solvent molecules from the pores while leaving the axial water molecule bound to the Cu(II) centre. The resultant MFM-170•H_2O was loaded with 1 bar SO_2, and subsequent refinement of the diffraction data gave a structure with formula $[Cu_2(L)(H_2O)_{0.79}](SO_2)_{3.27}$ (denoted MFM-170•H_2O•3.27SO_2). Of the six SO_2 molecules previously located in MFM-170•5.46SO_2, four are also present in MFM-170•H_2O•3.27SO_2 (Supplementary Fig. 26). Clearly, the Cu(II)-bound SO_2(2) site is absent in MFM-170•H_2O•3.27SO_2, and since SO_2(2) is a primary site of interaction for SO_2(5), the latter was not located either. However, the structural analysis shows that saturation of the Cu(II) sites in MFM-170 with H_2O does not greatly reduce the SO_2 binding capacity.

In situ spectroscopic analysis of host–guest binding dynamics

In situ FTIR spectroscopic studies of MFM-170 as a function of SO_2 loading (Fig. 6a–c) show growth of a new peak at 1,143 cm^{-1} (Fig. 6c) assigned to the ν_1 symmetric stretch of adsorbed SO_2, which increases as a function of SO_2 partial pressure (ppSO_2). This symmetric band is redshifted from 1,152 cm^{-1} (Δ = −9 cm^{-1}) for free SO_2, confirming its interaction with the framework. A second new band, assigned to the ν_3 asymmetric stretch of adsorbed SO_2, grows and redshifts from 1,340 cm^{-1} at 0.01 ppSO_2 to 1,320 cm^{-1} at 0.10 ppSO_2 (Fig. 6b). These bands show larger shifts compared with those of gas phase SO_2 (Δ = −41 cm^{-1} at 0.10 ppSO_2), but are consistent with physisorption of SO_2 (refs. [37,38]).

Significant vibrational changes in the framework were also observed on SO_2 adsorption. The carboxylate ν_{as}(COO) stretching mode at 1,658 cm^{-1} (Fig. 6a) and the ν_s(COO) stretching mode at 1,470 cm^{-1} (Fig. 6b) of MFM-170 decrease in intensity and are redshifted to 1,648 cm^{-1} (Δ = −10 cm^{-1}) and 1,462 cm^{-1} (Δ = −8 cm^{-1}) at 0.50 ppSO_2, respectively. This is distinct from the blueshifts of these bands observed in previously reported MOFs on SO_2 loading[19], probably due to the lack of OMSs in those reported structures. Furthermore, a redshift (Δ = −16 cm^{-1}) of the band at 1,595 cm^{-1} on SO_2 binding, assigned to the pyridine ring vibrational band ν(CC/CN), suggests a weakening of the pyridine N–Cu coordination on SO_2 adsorption[39].

In situ INS experiments were conducted for dry and wet MFM-170 to gain further insight into the dynamics of SO_2 binding (Fig. 6d–f, Supplementary Figs. 22–24). Comparing the spectra of bare MFM-170 and MFM-170•H_2O allows assignment of the water modes (Fig. 6d). The peak observed at 8.3 meV in the bare MOF can be attributed to a lattice mode which, on SO_2 loading, increases in intensity and shifts to 9.2 meV, suggesting a stiffening effect in MFM-170 on SO_2 binding (Fig. 6e). Overall, there is little change to the INS features of the MOF following SO_2 adsorption in MFM-170, indicating a moderate to weak host–guest interaction. Following SO_2 loading of MFM-170•H_2O, notable spectral changes are observed, which are attributed to interactions between bound water and SO_2 molecules (Fig. 6f). Subsequent activation of the SO_2-adsorbed MFM-170•H_2O at 373 K under vacuum removed all peaks assigned to water and led to a spectrum consistent with the dry, bare MOF, providing further evidence of the stability of the MOF to humid SO_2 (Supplementary Fig. 22).

Dynamic breakthrough separation of SO_2 in MFM-170

To test the effect of humidity on SO_2 adsorption in MFM-170, dynamic breakthrough experiments were conducted using either dry or wet simulated flue gas mixtures (Fig. 3c). Under dry conditions, breakthrough of SO_2 begins at dimensionless time τ = 420

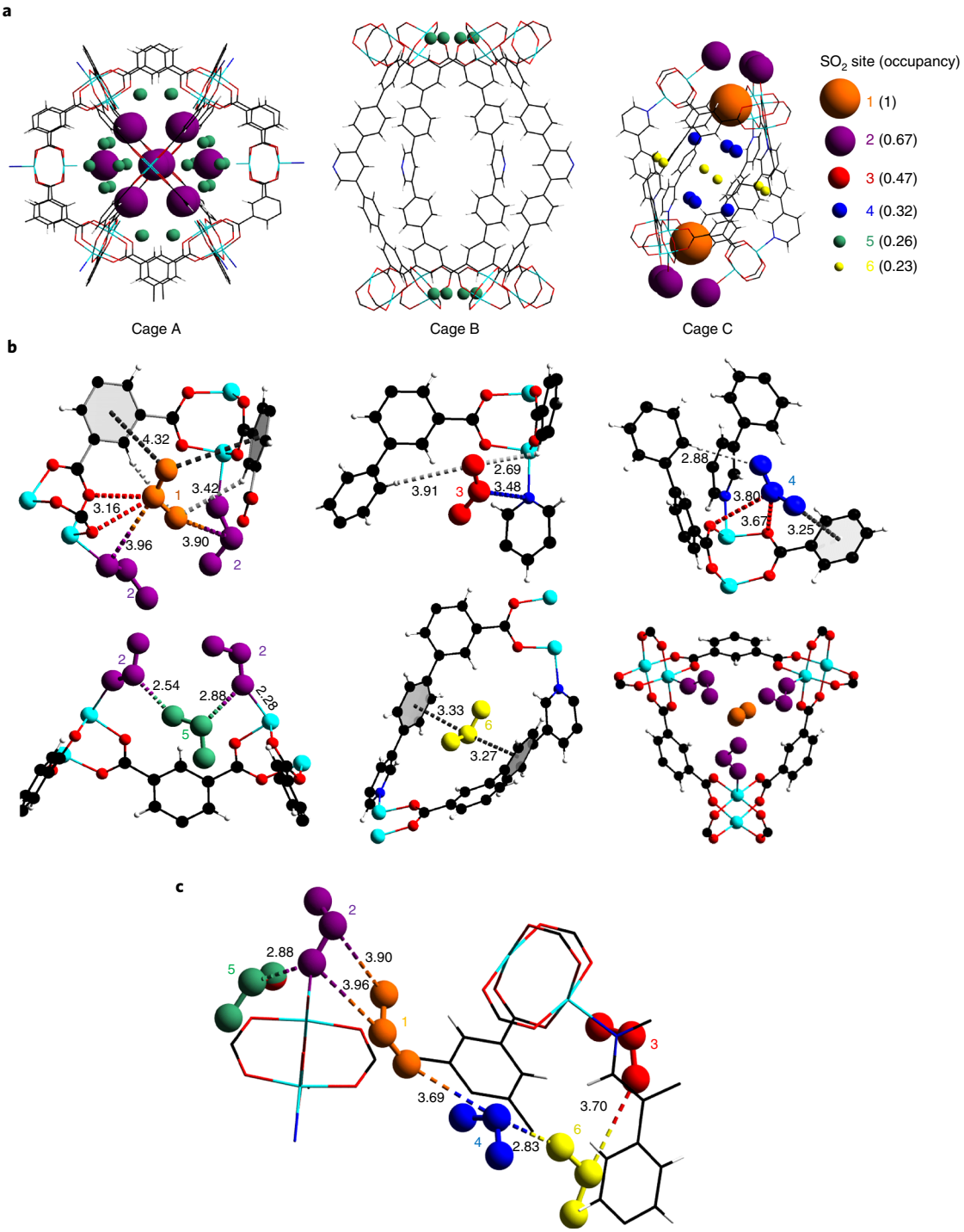

Fig. 5 | Positions of SO_2 molecules located within the pores of MFM-170•5.46SO_2 from in situ single-crystal X-ray diffraction. **a**, Packing of SO_2 within cages A, B and C. The smallest cage, C, accounts for ~45% of all located SO_2 molecules, while ~25% is found in the cuboctahedral cage A. No ordered SO_2 molecules were located in the largest cage, B, reflecting the large void space and lack of functional groups lining the pore. The sizes of the coloured balls depicting sites 1–6 are proportional to their occupancies. Site 3 is found in a crevice between two perpendicular B cages and is therefore not shown within the cages. **b**, Intermolecular interactions between adsorbed SO_2 molecules and MFM-170 framework atoms for binding sites 1–6. **c**, Intermolecular interactions between adsorbed SO_2 molecules. SO_2 molecules have been magnified slightly for clarity. Distances in **b** and **c** are in Å. Single-coloured dashed lines represent distances between adsorbed SO_2 molecules and framework atoms: red (O), blue (N), light grey (H), black (phenyl ring centroid). Dual-coloured dashed lines represent intermolecular interactions between crystallographically distinct SO_2 molecules.

and reaches a maximum by $\tau = 1{,}400$. With the addition of 1.5% H_2O, MFM-170 exhibits a slightly reduced SO_2 retention time at $\tau = 370$. Three cycles of SO_2 breakthrough and desorption (Fig. 3c) confirmed no significant deterioration in performance. To further investigate the separation ability for SO_2/CO_2, breakthrough experiments were carried out using simulated flue gas mixtures for a fully activated sample and a water-saturated sample of MFM-170 (Fig. 3d). For the dry sample, CO_2 is the first component eluted

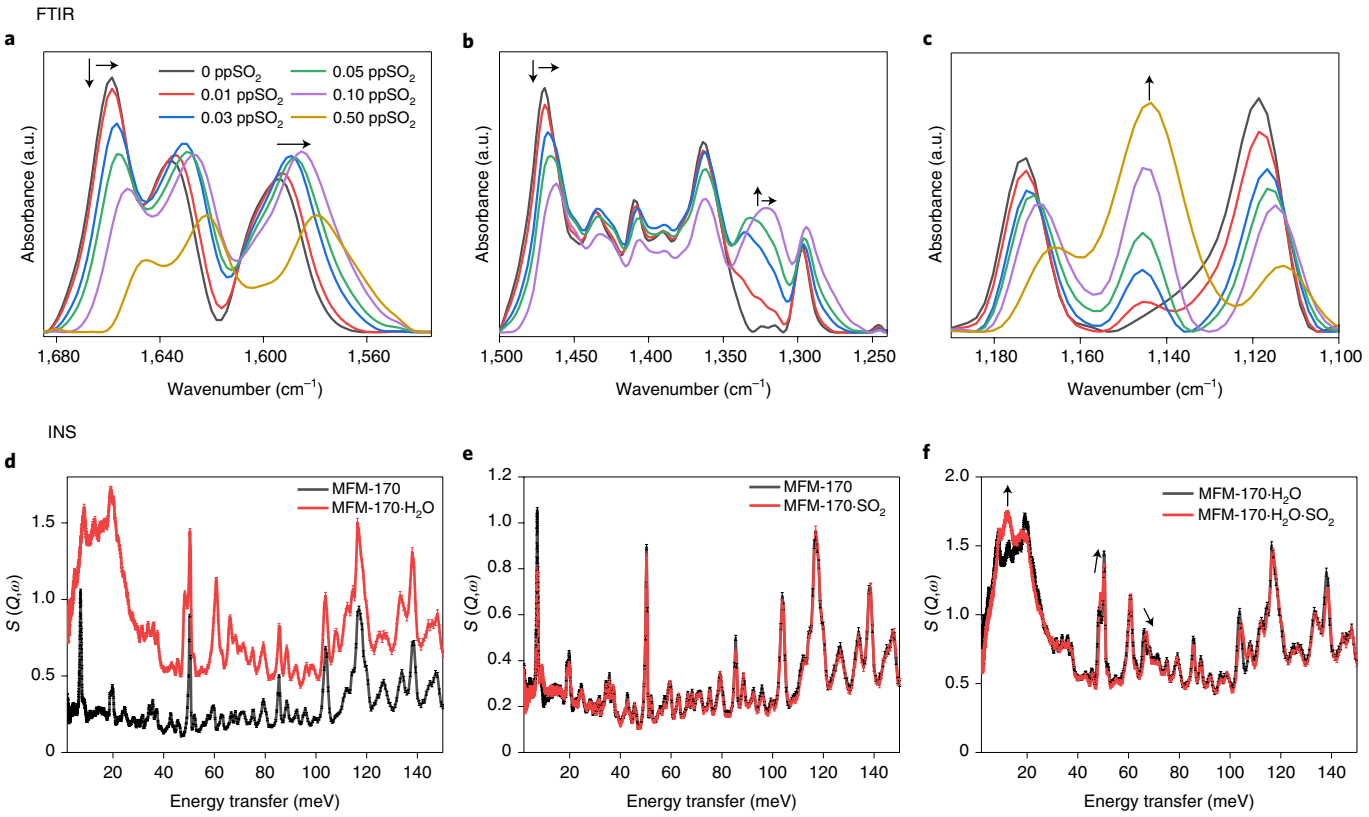

Fig. 6 | In situ vibrational spectra of MFM-170. a–c, FTIR spectra of MFM-170 at various SO_2 loadings up to 0.50 ppSO_2. **a**, Redshift of ν_{as}(COO) at 1,658 cm^{-1} and ν(CC/CN) at 1,595 cm^{-1}. **b**, Redshift of ν_s(COO) at 1,470 cm^{-1} and the ν_3 asymmetric stretch of adsorbed SO_2. **c**, Growth of a new band at 1,143 cm^{-1} assigned to the ν_1 symmetric stretch of adsorbed SO_2. All FTIR spectra were collected at 1.0 bar, using N_2 as a balancing gas. The fundamental ν_3 asymmetric stretch of gas phase SO_2 at 1,361 cm^{-1} saturates at low partial pressures in this experiment (Supplementary Fig. 21), and therefore the region of 1,400–1,300 cm^{-1} was monitored only up to 0.10 ppSO_2. **d–f**, INS spectra of MFM-170. **d**, Activated MFM-170 and MFM-170•H_2O. The additional peaks in MFM-170•H_2O are attributed to vibrational modes of water molecules: translational mode at 30 meV, rocking mode at 48 meV and wagging and twisting modes at 61 meV and 66 meV, respectively. **e**, The minimal difference between the two spectra, activated MFM-170 and MFM-170•SO_2. **f**, MFM-170•H_2O and MFM-170•H_2O•SO_2. Shifts in water modes are observed, indicating H_2O···SO_2 interactions.; the broad translational band at 30 meV increases in intensity, while the water rocking mode increases in intensity with a blueshift from 48 meV to 49 meV. The librational mode at 66 meV also blueshifts to 67 meV with a decrease in intensity.

through the fixed bed and breaks through at $\tau = 14$. In comparison, SO_2 is selectively retained by MFM-170 and breaks through much later ($\tau \approx 350$), with maximum output observed by $\tau = 1{,}450$. After breakthrough of SO_2, the packed bed was regenerated at 298 K under a helium flow, resulting in rapid desorption of both CO_2 and SO_2. No more SO_2 was detected in the effluent stream when the temperature was subsequently increased to 423 K, indicating the complete regeneration of MFM-170 at 298 K. The ability of MFM-170 to separate SO_2 from CO_2 in the presence of water was confirmed by repeating the breakthrough experiments with a water-saturated fixed bed. The column was exposed to a stream of 3% H_2O in He until breakthrough and saturation of water was observed. The subsequent breakthrough experiment demonstrated excellent SO_2/CO_2 separation under these conditions (Fig. 3d). While the breakthrough times were slightly decreased for both components compared with the times in the experiments under dry conditions, CO_2 is affected more severely with a much steeper breakthrough. Unlike the dry sample, a significant roll-up effect is observed for CO_2 under humid conditions, indicating a large displacement of weakly bound CO_2 by SO_2, probably due to the formation of H_2SO_3 complexes in the pore. This suggests that the SO_2/CO_2 separation in MFM-170 could be enhanced under humid conditions. Breakthrough experiments were also conducted for activated MFM-170 at elevated temperatures of 323 K and 348 K (Supplementary Fig. 25) to test suggested suitable temperature ranges for flue gas desulfurization processes[2,3]. A very clear separation between CO_2 and SO_2 is evident at both temperatures, but as expected, with reduced retention time.

Outlook

The development of efficient strategies to fully mitigate emissions of SO_2 and to achieve efficient SO_2 storage and safe transport remains a fundamental challenge for many industries and for power plants and marine transport sectors. Although MOF materials show great promise as sorbents for a wide range of inert gases, relatively little success has been achieved for the adsorptive removal of SO_2, primarily due to the generally limited reversibility and/or stability of MOFs on contact with highly corrosive SO_2. The present work describes a high SO_2 uptake of 17.5 mmol g^{-1} at ambient conditions in a remarkably stable MOF with open Cu(II) sites showing high selectivity for SO_2 over CO_2 and N_2. The binding sites of SO_2 in MFM-170 have been elucidated using in situ single-crystal X-ray diffraction, revealing the reversible coordination of SO_2 at open Cu(II) sites and five other binding sites. The open Cu(II) site has been identified as the thermodynamically favoured binding site for SO_2. In addition to static crystallography studies, dynamic vibrational modes were investigated using INS and FTIR microscopy as a function of SO_2 loading. The promise of MFM-170 has been demonstrated through dynamic breakthrough experiments, which showed efficient

separation of SO_2 from simulated flue gas mixtures, even in the presence of water and at elevated temperatures.

Online content

Any methods, additional references, Nature Research reporting summaries, source data, statements of code and data availability and associated accession codes are available at https://doi.org/10.1038/s41563-019-0495-0.

Received: 7 August 2018; Accepted: 29 August 2019;
Published online: 14 October 2019

References

1. Rezaei, F. et al. SO_x/NO_x removal from flue gas streams by solid adsorbents: a review of current challenges and future directions. *Energy Fuels* **29**, 5467–5486 (2015).
2. Gao, J. et al. Pilot-scale experimental study on the CO_2 capture process with existing SO_2: degradation, reaction rate, and mass transfer. *Energy Fuels* **25**, 5802–5809 (2011).
3. Ding, S. et al. Significant promotion effect of Mo additive on a novel Ce–Zr mixed oxide catalyst for the selective catalytic reduction of NO_x with NH_3. *ACS Appl. Mater. Interf.* **7**, 9497–9506 (2015).
4. Kinnunen, N. M. et al. Case study of a modern lean-burn methane combustion catalyst for automotive applications: what are the deactivation and regeneration mechanisms? *Appl. Catal. B Environ.* **207**, 114–119 (2017).
5. Han, X., Yang, S. & Schröder, M. Porous metal–organic frameworks as emerging sorbents for clean air. *Nat. Rev. Chem.* **3**, 108–118 (2019).
6. Raymundo-Piñero, E. et al. Factors controling the SO_2 removal by porous carbons: relevance of the SO_2 oxidation step. *Carbon* **38**, 335–344 (2000).
7. Mathieu, Y. et al. Adsorption of SO_x by oxide materials: a review. *Fuel Process. Technol.* **114**, 81–100 (2013).
8. Kohl, A. L. & Nielsen, R. *Gas Purification* (Gulf Professional, 1997).
9. Nabais, A. R. et al. CO_2/N_2 gas separation using Fe(BTC)-based mixed matrix membranes: a view on the adsorptive and filler properties of metal-organic frameworks. *Sep. Purif. Technol.* **202**, 174–184 (2018).
10. Peng, J. et al. Efficient kinetic separation of propene and propane using two microporous metal organic frameworks. *Chem. Commun.* **53**, 9332–9335 (2017).
11. Chen, D.-M. et al. Tunable robust pacs-MOFs: a platform for systematic enhancement of the C_2H_2 uptake and C_2H_2/C_2H_4 separation performance. *Inorg. Chem.* **57**, 2883–2889 (2018).
12. Zhong, R. et al. A solvent 'squeezing' strategy to graft ethylenediamine on $Cu_3(BTC)_2$ for highly efficient CO_2/CO separation. *Chem. Eng. Sci.* **184**, 85–92 (2018).
13. Zhang, Z. et al. MOFs for CO_2 capture and separation from flue gas mixtures: the effect of multifunctional sites on their adsorption capacity and selectivity. *Chem. Commun.* **49**, 653–661 (2013).
14. Peralta, D. et al. Comparison of the behavior of metal–organic frameworks and zeolites for hydrocarbon separations. *J. Am. Chem. Soc.* **134**, 8115–8126 (2012).
15. Carter, J. H. et al. Exceptional adsorption and binding of sulfur dioxide in a robust zirconium-based metal–organic framework. *J. Am. Chem. Soc.* **140**, 15564–15567 (2018).
16. Cui, X. et al. Ultrahigh and selective SO_2 uptake in inorganic anion-pillared hybrid porous materials. *Adv. Mater.* **29**, 1606929 (2017).
17. Glomb, S. et al. Metal–organic frameworks with internal urea-functionalized dicarboxylate linkers for SO_2 and NH_3 adsorption. *ACS Appl. Mater. Inter.* **9**, 37419–37434 (2017).
18. Yang, S. et al. Irreversible network transformation in a dynamic porous host catalyzed by sulfur dioxide. *J. Am. Chem. Soc.* **135**, 4954–4957 (2013).
19. Tan, K. et al. Mechanism of preferential adsorption of SO_2 into two microporous paddle wheel frameworks $M(bdc)(ted)_{0.5}$. *Chem. Mater.* **25**, 4653–4662 (2013).
20. Savage, M. et al. Selective adsorption of sulfur dioxide in a robust metal-organic framework material. *Adv. Mater.* **28**, 8705–8711 (2016).
21. Li, L. et al. Post-synthetic modulation of the charge distribution in a metal–organic framework for optimal binding of carbon dioxide and sulfur dioxide. *Chem. Sci.* **10**, 1472–1482 (2019).
22. Lee, G.-Y. et al. Amine-functionalized covalent organic framework for efficient SO_2 capture with high reversibility. *Sci. Rep.* **7**, 557 (2017).
23. Thallapally, P. K. et al. Prussian blue analogues for CO_2 and SO_2 capture and separation applications. *Inorg. Chem.* **49**, 4909–4915 (2010).
24. Fernandez, C. et al. Gas-induced expansion and contraction of a fluorinated metal−organic framework. *Cryst. Growth Des.* **10**, 1037–1039 (2010).
25. Tchalala, M. R. et al. Fluorinated MOF platform for selective removal and sensing of SO_2 from flue gas and air. *Nat. Commun.* **10**, 1328 (2019).
26. Riboldi, L. & Bolland, O. Overview on pressure swing adsorption (PSA) as CO_2 capture technology: state-of-the-art, limits and potentials. *Energy Proc.* **114**, 2390–2400 (2017).
27. Riboldi, L. & Bolland, O. Evaluating pressure swing adsorption as a CO_2 separation technique in coal-fired power plants. *Int. J. Greenh. Gas. Control* **39**, 1–16 (2015).
28. Britt, D. et al. Highly efficient separation of carbon dioxide by a metal-organic framework replete with open metal sites. *Proc. Natl. Acad. Sci. USA* **106**, 20637–20640 (2009).
29. Wong-Foy, A. G., Matzger, A. J. & Yaghi, O. M. Exceptional H_2 saturation uptake in microporous metal-organic frameworks. *J. Am. Chem. Soc.* **128**, 3494–3495 (2006).
30. Caskey, S. R., Wong-Foy, A. G. & Matzger, A. J. Dramatic tuning of carbon dioxide uptake via metal substitution in a coordination polymer with cylindrical pores. *J. Am. Chem. Soc.* **130**, 10870–10871 (2008).
31. Britt, D., Tranchemontagne, D. & Yaghi, O. M. Metal-organic frameworks with high capacity and selectivity for harmful gases. *Proc. Natl. Acad. Sci. USA* **105**, 11623–11627 (2008).
32. Guillerm, V. et al. A supermolecular building approach for the design and construction of metal–organic frameworks. *Chem. Soc. Rev.* **43**, 6141–6172 (2014).
33. Park, J. et al. A versatile metal–organic framework for carbon dioxide capture and cooperative catalysis. *Chem. Commun.* **48**, 9995–9997 (2012).
34. Lu, Z. et al. The utilization of amide groups to expand and functionalize metal-organic frameworks simultaneously. *Chem. A Eur. J.* **22**, 6277–6285 (2016).
35. Branton, P. J., Hall, P. G., Treguer, M. & Sing, K. S. W. Adsorption of carbon dioxide, sulfur dioxide and water vapour by MCM-41, a model mesoporous adsorbent. *J. Chem. Soc. Faraday Trans.* **91**, 2041–2043 (1995).
36. Tan, K. et al. Interaction of acid gases SO_2 and NO_2 with coordinatively unsaturated metal organic frameworks: MOF-74 (M = Zn, Mg, Ni, Co). *Chem. Mater.* **29**, 4227–4235 (2017).
37. Goodman, A. L., Li, P., Usher, C. R. & Grassian, V. H. Heterogeneous uptake of sulfur dioxide on aluminum and magnesium oxide particles. *J. Phys. Chem. A* **105**, 6109–6120 (2001).
38. Schneider, W. F., Li, J. & Hass, K. C. Combined computational and experimental investigation of SO_x adsorption on MgO. *J. Phys. Chem. B* **105**, 6972–6979 (2001).
39. Marinho, M. V. et al. Synthesis, crystal structure, and spectroscopic characterization of trans-bis[(μ-1,3-bis(4-pyridyl)propane)(μ-(3-thiopheneacetate-*O*))(3-thiopheneacetate-*O*)]dicopper(II), $\{[Cu_2(O_2CCH_2C_4H_3S)_4\ \mu\text{-}(BPP)_2]\}n$: from a dinuclear paddle-wheel copper(II) unit to a 2-D coordination polymer involving monatomic carboxylate bridges. *Inorg. Chem.* **43**, 1539–1544 (2004).

Acknowledgements

We thank EPSRC (EP/I011870), ERC (AdG 742041), the Royal Society and University of Manchester for funding. We are especially grateful to Diamond Light Source, Advanced Light Source, Oak Ridge National Laboratory and STFC/ISIS Neutron Facility for access to the beamlines B22/I11, 11.3.1, VISION and TOSCA, respectively. We thank M. Kibble for help at TOSCA beamline. The computing resources were made available through the VirtuES and the ICE-MAN projects, funded by the Laboratory Directed Research and Development programme at ORNL. This research used resources of the Advanced Light Source, which is a US Department of Energy Office of Science User Facility under contract no. DE-AC02-05CH11231. J.L. and X.Z. thank the China Scholarship Council (CSC) for funding.

Author contributions

G.L.S. and J.E.E. performed the synthesis and characterization of MOF samples and measurements of adsorption isotherms. G.L.S. and X.H. performed measurements and the analysis of the breakthrough data. G.L.S., X.Z., S.P.A., L.J.M., S.J.T. and S.Y. collected and analysed the synchrotron single-crystal X-ray diffraction data. G.L.S., H.G.W.G., Y.C., S.R. and A.J.R.-C. collected and analysed the neutron scattering data. G.L.S., S.J.D. and C.C.T. collected and analysed the long-duration synchrotron X-ray diffraction data. G.L.S., J.L., N.M.J., M.D.F., G.C. and T.L.E. collected and analysed the synchrotron IR data. T.L.E. supervised the laboratory work of J.E.E. S.Y. and M.S. led the overall design and direction of the project. G.L.S., S.Y. and M.S. prepared the manuscript with help from all authors.

Competing interests

The authors declare no competing interests.

Additional information

Supplementary information is available for this paper at https://doi.org/10.1038/s41563-019-0495-0.

Correspondence and requests for materials should be addressed to S.Y. or M.S.

Reprints and permissions information is available at www.nature.com/reprints.

Publisher's note Springer Nature remains neutral with regard to jurisdictional claims in published maps and institutional affiliations.

Methods

SO_2 safety. All systems involved in the supply, delivery and measurement of SO_2 were rigorously leak-tested and used only within range of a SO_2 detection system with a sensitivity of 0.1 ppm. All gases exhausted from experimental apparatus were diluted with a flow of N_2 and fed into fume hood extracts.

Synthesis of MFM-170•solv. $[Cu_2(C_{33}H_{17}NO_8)(H_2O)]$•6$(C_3H_7NO)$: H_4L (192 mg, 0.36 mmol) and $Cu(NO_3)_2$•2.5H_2O (298 mg, 1.28 mmol) were dissolved in a solution of DMF/H_2O (48 ml, 5:1) and acidified with concentrated HNO_3 (0.3 ml). The solution was heated in a Schott bottle at 80 °C for 18 h to form blue octahedral crystals. The product was filtered, washed with hot DMF and dried in air (320 mg, 86%). Attenuated total reflectance Fourier transform infrared spectroscopy (ATR-FTIR) revealed bands at the following wavenumbers (cm^{-1}): 3,382 (b, broad), 1,698 (w, weak), 1,645 (s, strong), 1,598 (s), 1,557 (s), 1,428 (s), 1,378 (vs, very strong), 1,298 (s), 1,244 (w), 1,170 (w), 1,116 (m, medium). Elemental analysis revealed the following compositions (% calculated/found): C, 53.46/52.93; H, 4.89/4.61; N, 6.93/7.18. Powder samples of MFM-170•H_2O•solv in this work were obtained by stirring identical reaction mixtures in a round bottom flask. Pawley refinement of the bulk powder sample of MFM-170 is shown in Supplementary Fig. 5. While the sum formula from single-crystal X-ray diffraction included in the refinement model is $Cu_2(C_{33}H_{17}NO_8)(H_2O)_{0.65}$, the final formula of $[Cu_2(C_{33}H_{17}NO_8)(H_2O)]$•6$(C_3H_7NO)$ was calculated from a combination of thermogravimetric analysis and elemental analysis, accounting for disordered solvent molecules.

Gas cell details and structure determination of MFM-170•H_2O•solv, MFM-170, MFM-170•5.46SO_2, MFM-170•0.09SO_2, MFM-170•H_2O and MFM-170•H_2O•3.27SO_2. Gas-loaded single-crystal X-ray diffraction experiments of MFM-170 were carried out at beamline 11.3.1 of the Advanced Light Source. Single crystals of MFM-170 were placed in a capillary gas handling cell and were evacuated in situ under a hot stream of N_2. The activated crystals were then cooled to ~300 K before being dosed with 1 bar of SO_2. The locations of the SO_2 molecules could be discerned from the Fourier difference maps at 300 K (MFM-170•5.46SO_2, MFM-170•0.09SO_2) and 260 K (MFM-170•H_2O•3.27SO_2) and were included in the refinement model with bond distances and angles constrained to ideal values. See the Supplementary Information for details of structure determination and refinement.

Crystal data for MFM-170•H_2O•solv. $[Cu_2(C_{33}H_{17}NO_8)(H_2O)_{0.65}]$; blue octahedron (0.1 × 0.1 × 0.1 mm). Cubic, *Im*-3*m*, a = 33.5294(17) Å, V = 37,963(7) Å^3, Z = 24, ρ_{calcd} = 0.729 g cm^{-1}. μ_{calcd} = 0.883 mm^{-1}, $F(000)$ = 8,413. A total of 45,304 reflections were collected, of which 1,475 were unique, giving R_{int} = 0.153. Final R_1 (wR_2) = 0.0465 (0.1226) with GoF = 1.130. The final difference Fourier extreme were 0.427 and −0.568 e Å^{-3}: a is the lattice parameter, V is the unit cell volume, Z is the number of formula units per unit cell, ρ_{calcd} is the calculated density, μ_{calcd} is the X-ray absorption coefficient, F is the structure factor, $R_{int}$is the error coefficient of collected data, R_1 and wR_2 are residual factors indicating how well the model fits the collected data, GoF is the goodness of fit.

Crystal data for desolvated MFM-170. $[Cu_2(C_{33}H_{17}NO_8)]$; purple octahedron (0.1 × 0.1 × 0.1 mm). Cubic, *Im*-3*m*, a = 33.609(2) Å, V = 37,694(6) Å^3, Z = 24, ρ_{calcd} = 0.722 g cm^{-1}. μ_{calcd} = 0.883 mm^{-1}, $F(000)$ = 8,256. A total of 42,452 reflections were collected, of which 1,043 were unique, giving R_{int} = 0.197. Final R_1 (wR_2) = 0.039 (0.097) with GoF = 1.045. The final difference Fourier extremes were 0.320 and −0.381 e Å^{-3}.

Crystal data for MFM-170•5.46SO_2. $[Cu_2(C_{33}H_{17}NO_8)(SO_2)_{0.67}](SO_2)_{4.79}$; blue octahedron (0.1 × 0.1 × 0.1 mm). Cubic, *Im*-3*m*, a = 33.5808(17) Å, V = 37,868(6) Å^3, Z = 24, ρ_{calcd} = 1.086 g cm^{-1}. μ_{calcd} = 1.144 mm^{-1}, $F(000)$ = 12,448. A total of 105,823 reflections were collected, of which 2,202 were unique, giving R_{int} = 0.186. Final R_1 (wR_2) = 0.117 (0.331) with GoF = 1.663. The final difference Fourier extremes were 1.577 and −1.156 e Å^{-3}.

Crystal data for MFM-170•0.09SO_2. $[Cu_2(C_{33}H_{17}NO_8)(SO_2)_{0.09}]$; blue octahedron (0.1 × 0.1 × 0.1 mm). Cubic, *Im*-3*m*, a = 33.5458(19) Å, V = 37,750(6) Å^3, Z = 24, ρ_{calcd} = 0.727 g cm^{-1}. μ_{calcd} = 0.890 mm^{-1}, $F(000)$ = 8,324. A total of 73,416 reflections were collected, of which 1,471 were unique, giving R_{int} = 0.173. Final R_1 (wR_2) = 0.0411 (0.092) with GoF = 1.083. The final difference Fourier extremes were 0.517 and −0.474 e Å^{-3}.

Crystal data for MFM-170•H_2O. $[Cu_2(C_{33}H_{17}NO_8)(H_2O)_{0.50}]$; blue octahedron (0.1 × 0.1 × 0.1 mm). Cubic, *Im*-3*m*, a = 33.4562(16) Å, V = 37,448(5) Å^3, Z = 24, ρ_{calcd} = 0.736 g cm^{-1}. μ_{calcd} = 0.895 mm^{-1}, $F(000)$ = 8,376. A total of 110,623 reflections were collected, of which 2,211 were unique, giving R_{int} = 0.0699. Final R_1 (wR_2) = 0.0565 (0.1799) with GoF = 1.124. The final difference Fourier extremes were 0.702 and −0.458 e Å^{-3}.

Crystal data for MFM-170•H_2O•3.27SO_2. $[Cu_2(C_{33}H_{17}NO_8)(H_2O)_{0.79}](SO_2)_{3.27}$; blue octahedron (0.1 × 0.1 × 0.1 mm). Cubic, *Im*-3*m*, a = 33.610(4) Å, V = 37,968(12) Å^3, Z = 24, ρ_{calcd} = 0.951 g cm^{-1}. μ_{calcd} = 1.039 mm^{-1}, $F(000)$ = 10,957. A total of 84,668 reflections were collected, of which 1,720 were unique, giving R_{int} = 0.078. Final R_1 (wR_2) = 0.0947 (0.3006) with GoF = 1.529. The final difference Fourier extremes were 0.909 and −0.618 e Å^{-3}.

A more detailed description of the single-crystal X-ray diffraction data and analysis can be found in the Supplementary Information.

Gas adsorption isotherms and breakthrough experiment. Measurements of SO_2 adsorption isotherms (0–1 bar) were performed using a Xemis gravimetric adsorption apparatus (Hiden Isochema) equipped with a clean ultrahigh vacuum system. The pressure in the system was accurately regulated by mass flow controllers. Research-grade SO_2 and He were purchased from AIRLIQUIDE or BOC and used as received. In a typical gas adsorption experiment, 70–100 mg of MFM-170•H_2O•solv was loaded into the Xemis and degassed at 423 K and high dynamic vacuum (10^{-10} bar) for 1 day to give desolvated MFM-170. Calculated heats of adsorption (Q_{st}) are shown in Supplementary Figs. 16–18.

Breakthrough experiments were carried out in a 7-mm-diameter fixed-bed tube of 120 mm length packed with 1.5 g of MFM-170 powder (particle size <5 μm). The total volume of the bed was ~5 cm^3. The sample was heated at 423 K under a flow of He for 2 days for complete activation. The fixed-bed was then cooled to room temperature (298 K) using a temperature-programmed water bath, and the breakthrough experiment was performed with streams of SO_2 (0.5% diluted in He) and CO_2 at atmospheric pressure and room temperature. The flow rate of the entering gas mixture was maintained at 47 ml min^{-1}, and C of SO_2 and CO_2 was determined by mass spectrometry and compared with the corresponding C_0, where C/C_0 = 1 indicates complete breakthrough. A more detailed description is given in the Supplementary Information.

Data availability

Results of the refinements of the solvated, evacuated and SO_2-loaded crystal structures of MFM-170 have been deposited as CIF files with CCDC numbers 1538125–1538126, 1538129 and 1853512–1853514. These data can be obtained free of charge from https://www.ccdc.cam.ac.uk/structures/.